An All-Solid-State Flexible Piezoelectric High-*k* Film Functioning as Both a Generator and In Situ Storage Unit

Wangshu Tong, Yihe Zhang, Qian Zhang, Xinglong Luan, Fengzhu Lv, Leipeng Liu, and Qi An**

An all-solid-state flexible generator–capacitor polymer composite film converts low-frequency biomechanical energy into stored electric energy. This design, which combines the functionality of a generator with a capacitor, is realized by employing poly(vinylidene fluoride-*co*-hexafluoropropylene) (PVDF-HFP) in the simultaneous dual role of piezoelectric generator and polymer matrices of the flexible capacitor. Proper surface modification of the reduced graphene oxide (rGO) fillers in the polymeric matrices is indispensable in achieving the superior energy storage performance of the composite film. The heightened dielectric performance stems from enhanced compatibility of the rGO fillers and PVDF-HFP matrices, and a microcapacitor model properly explains the dielectric behaviors. A device that is easily fabricated using our film allows timely decoupled motion energy harvest and output of the motion-generated electricity. This report opens new design possibilities in the fields of motion sensors, information storage and high-voltage output by accumulating low-frequency random biological motions.

1. Introduction

Energy conversion and storage are two core issues in sustainable development for enhancing the quality of human life.[1–3] The development of flexible tribo- and piezoelectic nanogenerators has tremendously improved researchers' ability to convert low-frequency biomechanical movement into electricity.[2–13] At the same time, the flexibility and miniaturization of electric storage devices, such as batteries and (super) capacitors, have also significantly developed over time.[14–20] Though effectively harnessing biomechanical energy for electric power requires both energy conversion and storage devices, these two types of devices (generators and storage units) have largely been developed without much intersection. Only recently, pioneering researchers have integrated a flexible nanogenerator with flexible storage devices (self-charging power cells), and, as a result, mechanical energy was converted and directly stored as electrochemical energy.[21,22]

In addition, the application conditions of the motion-harvesting devices require an all-solid-state design in order to avoid leakage and guarantee safe applications. While devices that simultaneously meet these requirements are highly appealing, at the same time, an all-solid-state flexible generator that converts ambient environmental motions into stored electric energy is very challenging to fabricate. Ramadoss et al. recently reported on such a functionally integrated device which they created by integrating the piezoelectric film with an all-solid-state lithium battery.[23] In our study, we achieved a solid-state flexible piezoelectric generator-and-capacitor film by using an entirely new mechanism. This mechanism allowed us to convert low-frequency biomechanical energy into stored electricity in capacitors as shown in **Figure 1**a–d. The core of our device was a high-*k* flexible piezoelectric composite film prepared from poly(vinylidene fluoride-*co*-hexafluoropropylene) (PVDF-HFP) as matrices and reduced graphene oxide (rGO) as fillers as shown in Figure 1e,f. PVDF-HFP served a simultaneous dual role: 1) the piezoelectric unit for the generator and 2) the polymeric matrices for the high-*k* film in the capacitor.

The key issue for achieving high performance of electric storage was the chemical modification of rGO fillers with 4-azidotetrafluorobenzoic acid (TFB) in order to enhance permittivity and keep the electric loss of the film at low values.[24–29] The advantageous dielectric performance of our film was achieved by enhancing the compatibility of rGO fillers and PVDF-HFP matrices. In addition, a microcapacitor model properly explained the dielectric behavior of our composite film. The in situ storage ability of our device allowed timely decoupled motion-energy harvest as well as the output of motion-generated electricity. Different from previous reports, in our study, electric energy was stored in capacitors instead of batteries. This report establishes linkage of the field of PVDF-based piezoelectric generators and the discipline of flexible high-*k* composite films. These unique features of our simply fabricated device should potentially enhance new possibilities in the fields of sensor applications, information storage, and flexible high-voltage output designs.

Dr. W. Tong, Prof. Y. Zhang, Dr. Q. Zhang, Dr. X. Luan, Dr. F. Lv, Dr. L. Liu, Dr. Q. An
Beijing Key Laboratory of Materials Utilization of Nonmetallic Minerals and Solid Wastes
National Laboratory of Mineral Materials
School of Materials Sciences and Technology
China University of Geosciences
Beijing 100083, P. R. China
E-mail: zyh@cugb.edu.cn; an@cugb.edu.cn

DOI: 10.1002/adfm.201503514

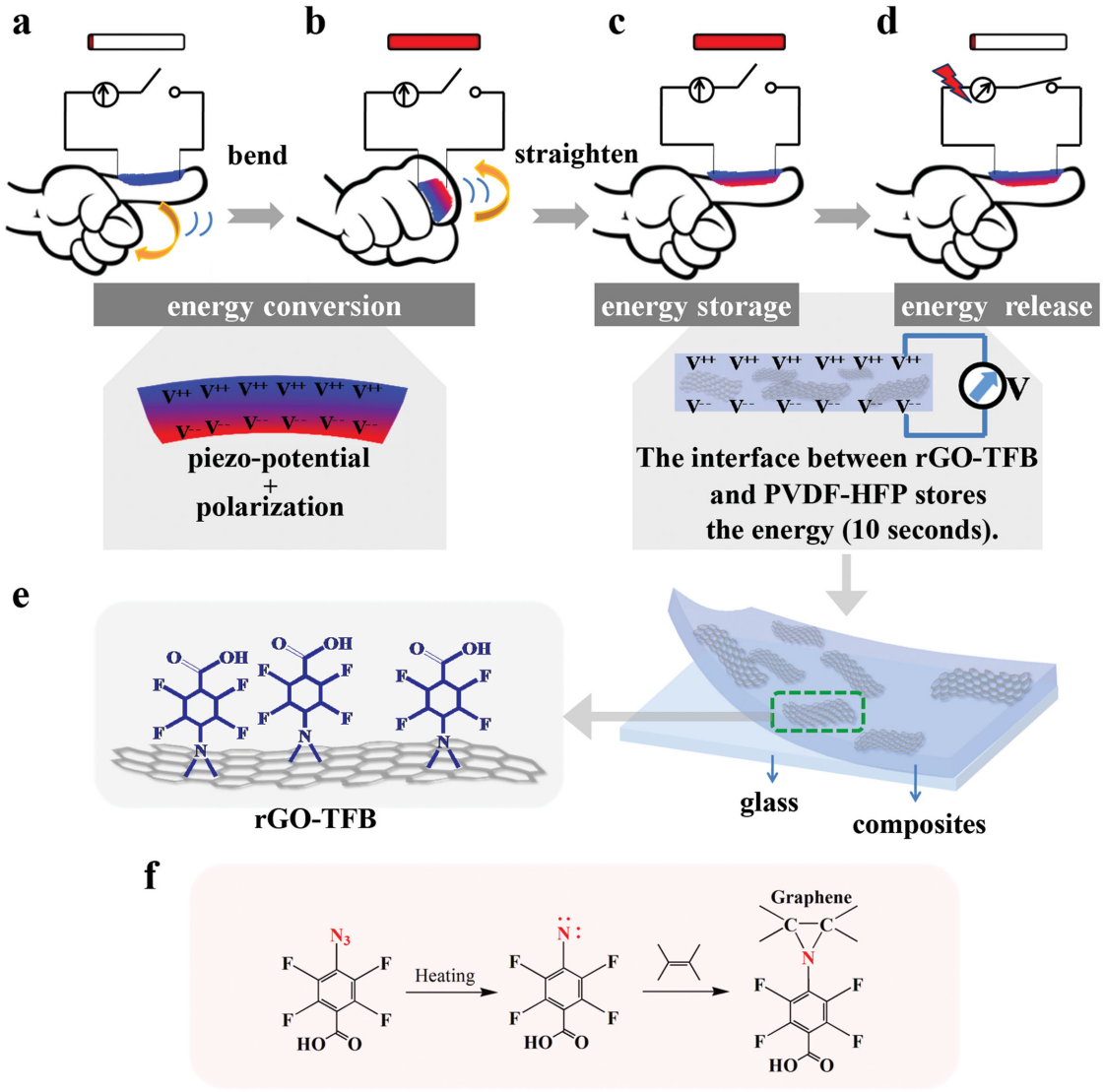

Figure 1. Schematic illustrations of energy conversion and storage. Schematic illustrations of a–d) energy conversion and storage by nanocomposite films under biological motions and e,f) the rGO-TFB/PVDF-HFP nanocomposite and the mechanism of reaction between TFB and graphene.

2. Results and Discussions

2.1. Modifying rGO Filler Surface

Previous elegant studies have demonstrated that proper surface modification of rGO fillers is the key issue when enhancing the dielectric performance of a composite film.[24–29] However, the choice of an appropriate surface modification strategy continues to remain challenging. We chose a small molecule TFB to modify rGO surfaces in order to effectively enhance the compatibility between the fillers and the matrices. Consequently, we obtained a high-permittivity–low-loss dielectric film. The successful functionalization of graphene by TFB was confirmed by Fourier transform infrared spectroscopy (FTIR) spectroscopy. **Figure 2**a shows the FTIR spectra of the GO, rGO-TFB, and TFB. The intense absorption bands at 2136 and 1263 cm^{-1} in TFB were the asymmetric and symmetric stretching vibrations of N=N=N, respectively.[30] The vibrational bands at 1715, 1646, 1491, and 1423 cm^{-1} were characteristic of benzene ring in TFB. Peaks at 1197 cm^{-1} were assigned to the C–F symmetric vibrations and, at 1735 cm^{-1}, the peaks corresponded to C=O in carboxylic acid. The rGO-TFB presented the characteristic peaks of a benzene ring, C–F bonds, and C=O bonds, indicating the attachment of TFB onto rGO surfaces. In addition, the strong vibrational band corresponding to azide groups (2136 cm^{-1}) was absent in the rGO-TFB spectra, indicating that the azide groups were decomposed. This decomposition was consistent with the hypothesis that TFB attached to rGO via the reaction between azide groups and C=C bonds in rGO.[30,31]

The X-ray photoelectron spectroscopy (XPS) survey spectra in Figure 2b presented peaks of N1s and F1s for rGO-TFB, demonstrating the successful functionalization of rGO by TFB as well. High-resolution XPS C1s and N1s core-level spectra of rGO-TFB are displayed in Figure 2c,d. Curve fitting indicated

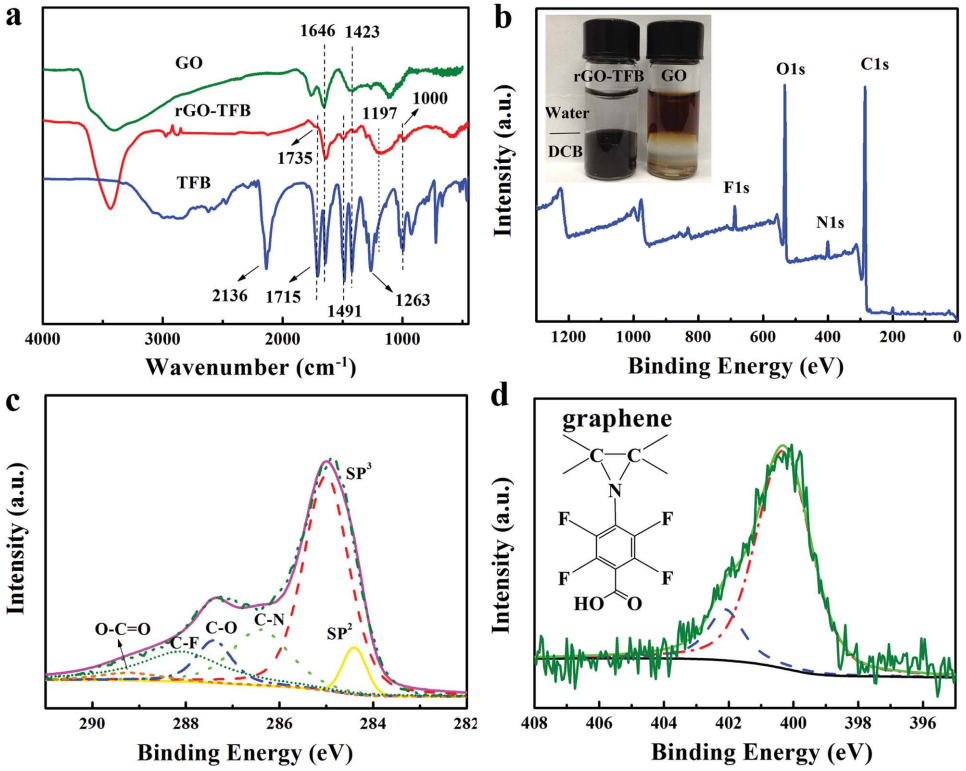

Figure 2. FTIR and XPS spectra of rGO-TFB. a) FTIR spectra of GO, rGO-TFB and TFB and b) XPS survey spectra of rGO-TFB and the inserted photo images about GO and rGO-TFB in the mixed solvents of water (top layer) and DCB (bottom layer). c) High-resolution XPS C1s core-level spectra of rGO-TFB and d) high-resolution XPS N1s core-level spectra of rGO-TFB.

that the C1s spectrum of the rGO-TFB sheets could be quantitatively differentiated into six different carbon species: the sp^2-hybridized carbon atoms of graphene at 284.4 eV (C–C sp^2), the sp^3-hybridized carbon atoms at 285.0 eV (C–C sp^3),the C–N of 286.4 eV,[32] the carbon in epoxide groups (C–O) at 287.4 eV, the phenyl-CF at 288.1 eV (C–F)[32] and those in carboxyl groups (O–C=O) at 289.2 eV.[33,34] The coexistence of characteristic peaks in both rGO and TFB indicated that TFB was grafted on rGO surfaces.[32]

The N1s core-level spectra in Figure 2d consist of two components with binding energies of 402.1[32,35] and 400.3 eV. The peak at 400.3 eV corresponded to the N in amides, and the source for the peak at 402.1 eV was debatable. The position, shape, and the ratio of the N 1s spectra confirmed that TFB was covalently grafted onto rGO surfaces.[32,36,37] The image inserted into Figure 2b indicates the alteration of solubility of rGO before and after chemical modification of TFB. Before the chemical modification, GO dispersed homogeneously in water. In contrast, rGO-TFB dispersed in 1,2-dichlorobenzene (DCB), but not in water. The drastic change of the wettability served as strong evidence that the graphene was functionalized with TFB.[38]

The uniform distribution of the grafted TFB on the rGO surfaces was indicated by an elemental mapping measurement. **Figure 3** indicates that the area covered by N and F elements that stemmed from TFB molecules roughly overlapped the area observed for the rGO-TFB sample in the scanning electron microscopy (SEM) image and presented small concentration fluctuations throughout the image. The EDX (Energy Dispersive X-Ray) analysis indicated the content of carbon, oxygen, nitrogen, and fluorine elements as shown in Figure 3e. The grafting weight density of TFB calculated by TGA (Thermogravimetric Analysis) measurement was 5.8 wt% (for detailed calculation see Figure S1 and Section 1 in the Supporting Information). This result was consistent with elemental fractions obtained by EDX and XPS analysis (Tables S1 and S2, Supporting Information). These grafting density results indicated that the ratio of C–F bond in TFB to C atom in rGO was ≈3%. These C–F bonds on rGO surface should effectively enhance filler-matrix compatibility, as verified by TGA measurement of the composite film in the next section, because of their high consistency in polarity with C–F bonds in PVDF-HFP matrices.[39,40]

2.2. TGA Analysis of PVDF-HFP Compatibility with Nanocomposites

After covalent modification of rGO by TFB, its compatibility with PVDF-HFP matrices remarkably improved as indicated by TGA analysis. TGA of pure PVDF-HFP, rGO/PVDF-HFP, and rGO-TFB/PVDF-HFP nanocomposites are shown in **Figure 4**. The major weight loss of all the samples took place from ≈425 to 500 °C, which was assigned to the decomposition of the PVDF-HFP matrix for all three samples. However, the onset of the decomposition temperatures differed for the three samples. The decomposition temperature of rGO-TFB/PVDF-HFP was the highest (470 °C) followed by that of rGO/PVDF-HFP

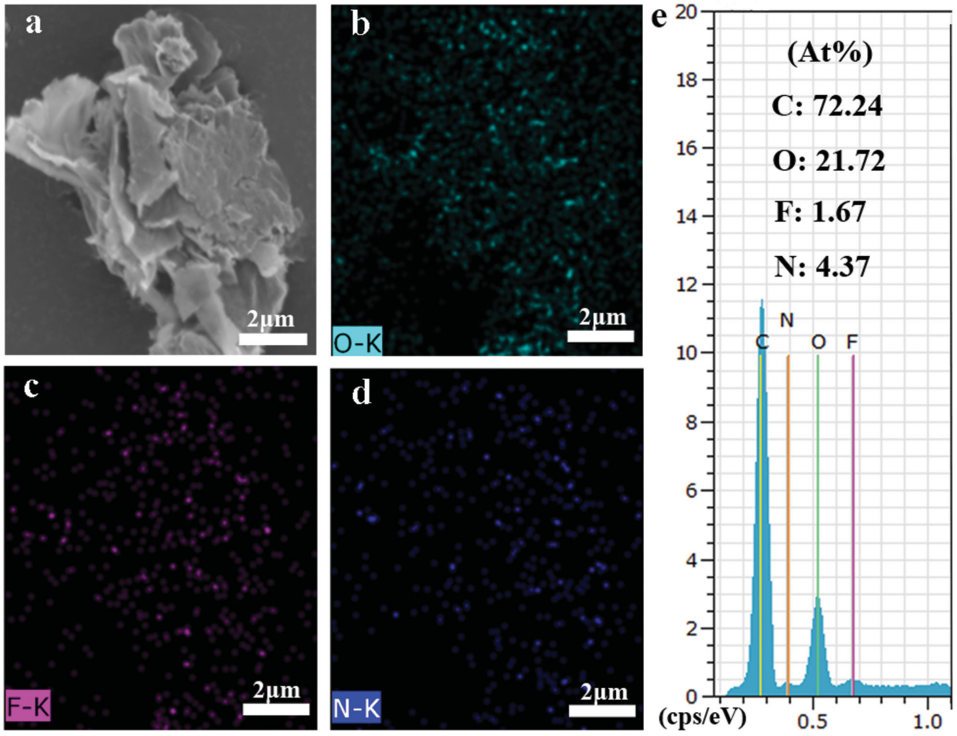

Figure 3. Elemental mapping images of rGO-TFB. a) A typical SEM image and the corresponding elemental mapping images of b) oxygen, c) fluoride, and d) nitrogen, indicating the homogeneous dispersion of O, F, and N in rGO-TFB. e) The EDX analysis of carbon, oxygen, nitrogen, and fluorine elements.

(467 °C). The decomposition temperature of pure PVDF-HFP was the lowest (460 °C). The differences in the decomposition temperatures can be explained as follows: i) the introduction of rGO nanosheets restricted the thermal motions of the polymer chains, effectively promoting the thermal stability of the polymer matrix[24] and ii) functional groups of TFB presented stronger intermolecular interactions toward the PVDF-HFP matrix and thus further increased restrictions of polymeric chain movement, leading to higher decomposition temperatures.[41]

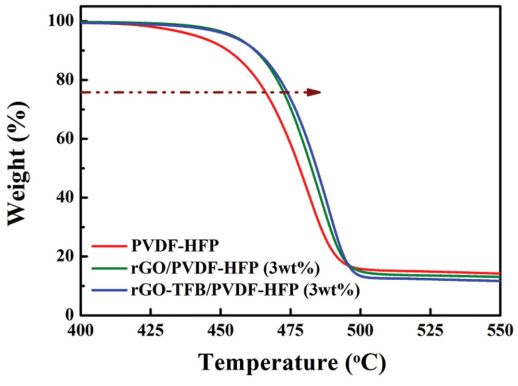

Figure 4. TGA curves of pure PVDF-HFP, rGO/PVDF-HFP, and rGO-TFB/PVDF-HFP nanocomposites.

Differential scanning calorimetry (DSC) and FTIR indicated that the fillers altered the crystal structures of the PVDF-HFP matrices as shown in **Figure 5**. During the cooling process, the crystallization temperatures (T_c) of the nanocomposites shifted to higher temperatures upon the introduction of the rGO and rGO-TFB fillers. The T_c of the pure PVDF-HFP was 97 °C, whereas the T_c value increased to 106 °C for the composite film with 3.0 wt% of rGO fillers and to 101 °C for the rGO-TFB fillers. The shift of the crystallization peak toward higher temperatures suggested a heterogeneous nucleation effect induced by rGO and rGO-TFB fillers. Higher temperature is required to crystallize the β phase of PVDF-HFP, so we can deduce from T_c during the cooling process that rGO/PVDF-HFP presented the highest fraction of the β phase out of the three types of composite films. This is consistent with FTIR results displayed in Figure 5b–d.

The FTIR spectra of rGO-TFB/PVDF-HFP with the filler fraction from 0.5 to 1.5 wt% clearly indicated that the α and β phases coexisted in the rGO/PVDF-HFP and rGO-TFB/PVDF-HFP nanocomposites as well as the pure PVDF-HFP films.[42,43] Increased amounts of rGO-TFB nanosheet fillers slightly increased the fraction of the β-phase in the composite (Figure 5b). In comparison, the rGO filler induced a larger fraction of the β-phase in the composite (Figure 5c,d) as indicated by the vibrational bonds at around 840 cm^{-1}. These results indicated that both rGO and rGO-TFB fillers induced structural changes of the composite films, but rGO-TFB presented different intermolecular interactions with the matrix polymer chains than rGO did.

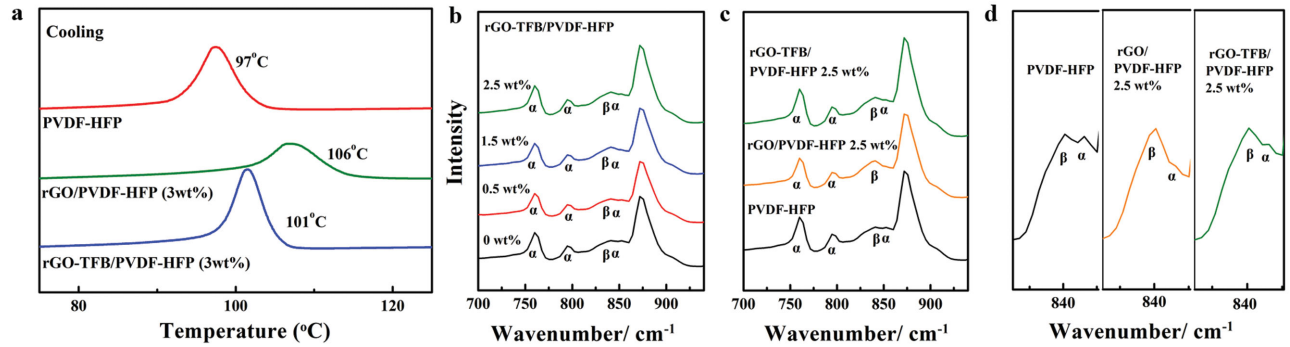

Figure 5. DSC and FTIR analysis. a) DSC cooling curves of pure PVDF-HFP, rGO/PVDF-HFP, and rGO-TFB/PVDF-HFP nanocomposites, b) FTIR spectra of rGO-TFB/PVDF-HFP with 0, 0.5, 1.5, and 2.5 wt% of rGO-TFB, c) FTIR spectra of rGO-TFB/PVDF-HFP (2.5 wt%) compared with rGO/PVDF-HFP (2.5 wt%) and pure PVDF-HFP, and d) the enlarged image for bonds around 840 cm^{-1} of sample pure PVDF-HFP, rGO/PVDF-HFP (2.5 wt%), and rGO-TFB/PVDF-HFP (2.5 wt%).

2.3. Morphological Changes of Nanocomposites

SEM images of the cross-sections of the films (as depicted in **Figure 6**) indicated morphological changes of rGO-TFB/PVDF-HFP when compared with the pure PVDF-HFP films. The cross-section image for the rGO-TFB/PVDF-HFP composite displayed layered features that were absent in the image of pure PVDF-HFP, but the distribution of the layered features was homogeneous throughout the image. This result was consistent with the structural changes induced by the rGO-TFB fillers as indicated by the DSC and FTIR spectra. The homogeneous cross-section image of the rGO-TFB/PVDF-HFP composite without any aggregations also supported the argument that TFB presented strong interactions with the PVDF-HFP matrix that, in turn, led to high compatibility between the fillers and the matrices.[24,44]

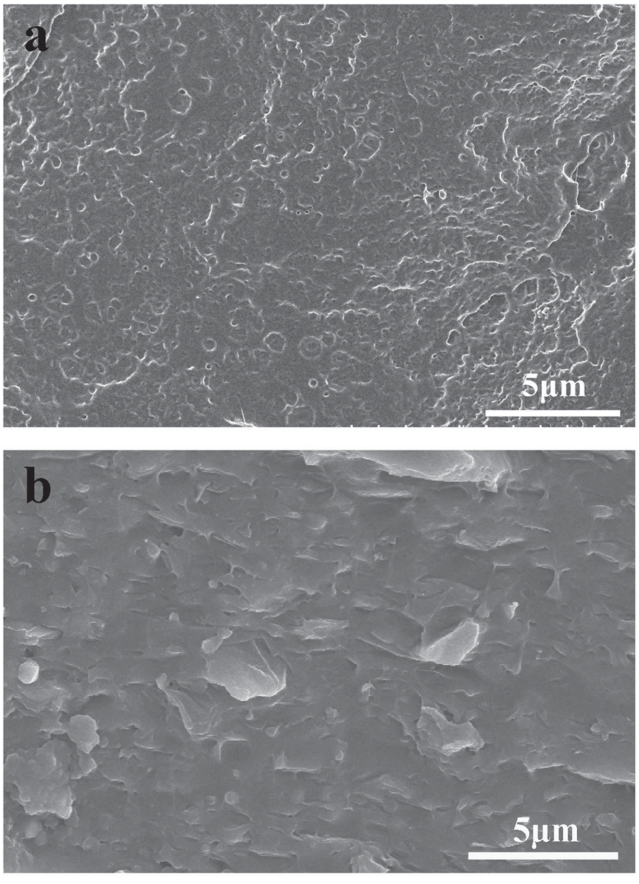

Figure 6. SEM image of the cross section of a) pure PVDF-HFP and b) 2.0 wt% rGO-TFB/PVDF-HFP.

2.4. Dielectric Properties of rGO-TFB/PVDF-HFP Composite

We further studied the dielectric properties of the rGO-TFB/PVDF-HFP composite between 10^2 and 10^6 Hz at room temperature. The dielectric constants and losses of the composite films were documented as a function of frequency with different weight fractions of rGO-TFB fillers. Over the entire tested frequency range from 100 Hz to 4 MHz, up until the volume fractions of 2.2 wt%, the dielectric constant increased only slightly with the increase of the fraction of rGO-TFB so long as the loss (Tan δ) was kept as low as 0.17 (as shown in **Figure 7**). The large enhancement of dielectric constant at low frequencies was mainly attributed to the Maxwell–Wagner–Sillars interfacial polarization due to the different conductivity of rGO-TFB and PVDF-HFP.[39] When the rGO-TFB fractions were higher than 2.2 wt%, the dielectric constants first increased remarkably with filler fractions and then decreased and presented a strong dependence on frequency, especially at low frequency ranges. In the meantime, the loss also increased rapidly when the filler fraction was larger than 2.3 wt% and reached the value of 0.7 when the filler fraction was 3 wt%. An optimized dielectric performance with a dielectric constant of 158 and loss of 0.42 (100 Hz) was achieved when the filler fraction was 2.5 wt%. In comparison, rGO/PVDF-HFP presented higher dielectric constants but also significantly higher dielectric losses (the dielectric constant and loss of 2.5 wt% rGO/PVDF-HFP were 10 089 and 802, respectively) as reported in our previous work.[40]

The performance differences caused by different filler types were explained as follows. On rGO surfaces, the covalently attached TFB molecules presented strong intermolecular interactions with the matrices polymer PVDF-HFP. As a result, not

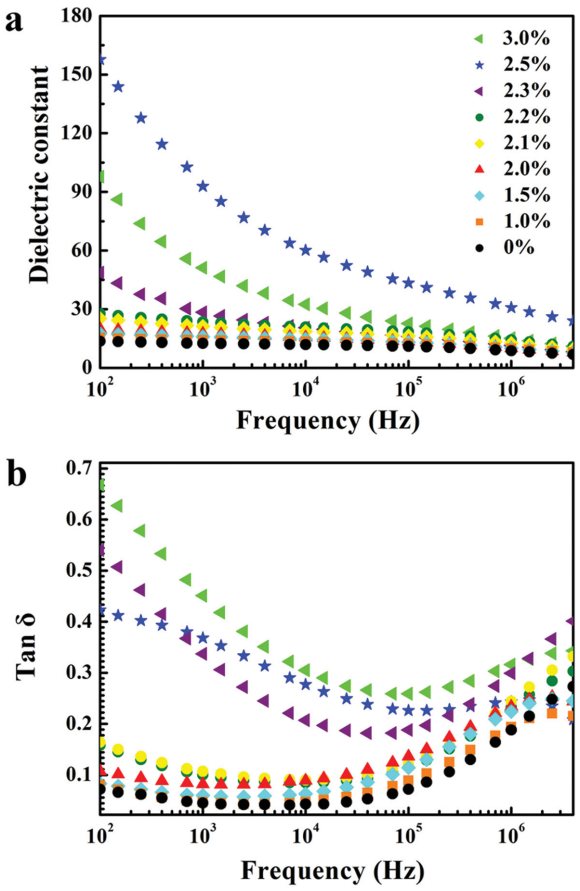

Figure 7. Frequency response of a) the dielectric constants and b) dielectric losses of the rGO-TFB/PVDF-HFP composites.

only TFB itself but also a thin layer of matrices polymer PVDF-HFP was quasi-immobilized around the rGO cores. The existence of the organic species around rGO served as the insulating layer between two adjacent rGO sheets. By such an arrangement, numerous microcapacitors comprised of rGO sheets and the insulating polymer layers in between the rGO sheets were formed within the polymeric composite. Good compatibility minimized the shortest possible distance between the two adjacent rGO sheets before uneven distribution was reached. Good compatibility also allowed large values for each microcapacitor, maximized the number of existing microcapacitors in the composite films and, at the same time, kept the dielectric losses at low values. In comparison, rGO without surface modification or with noncovalent surface modification as the filler presented poor interfacial compatibility with the polymer matrices and, consequently, could not achieve the optimized dielectric performance as rGO-TFB fillers (as studied in our previous work and shown in Figure S2 in the Supporting Information).[40]

2.5. The Device with Dual Roles of Generator and Capacitor

Furthermore, taking advantage of the piezoelectric properties of the β-phase PVDF and the high dielectric constant–low-loss characteristics of our composite film, a functionally integrated device that simultaneously converted low-frequency biomechanical energy into electric energy and stored the generated electric energy was demonstrated. The device (shown in **Figure 8**a, fabricated with filler fraction 2.5%, and β-phase fraction therein was 42% calculated from FTIR measurements as detailed in Section 3 in the Supporting Information) was a piece of our composite film to which we attached two pieces of parallel Cu foils to the top and bottom surfaces. These Cu foils served as the charge collectors and Cu wires were attached onto the Cu foils in order to connect our device into an electric circuit. The device was fixed onto a finger of a plastic disposable glove. The mechanical energy of the finger as it bent was harvested by the device, and output currents corresponding to finger movements were observed as shown in Figure 8a. The ability to harvest mechanical energy and convert it into electric energy justified our device as a nanogenerator.

In order to demonstrate the device's ability to store the electric energy, we decoupled the energy harvest (conversion) and the energy output processes by conducting the charging and discharging experiments at different time points. The device was disconnected from the circuit during finger movements, and in this process, the mechanical energy was only converted into electric energy and not exported from the device as shown in Figure 8b. Because of the dielectric nature of the composite film, the converted electric energy could be stored in situ, and when the device was connected to the circuit after the finger movements by an 8 s delay, the stored electric energy could be exported as electric signals. In comparison, the pure PVDF-HFP film with a much lower dielectric constant could only express the electric signals at much lower magnitudes.

The difference in output values of the current for the composite film and PVDF-HFP film was attributed to their different dielectric constant (158 vs 13). Short circuit current outputs were similar for the pure PVDF-HFP films and our composite films when measured in closed circuits in situ (current outputs are shown in Figure S4 in the Supporting Information). However, our composite film with a larger dielectric constant exported remarkably larger current values when measured in timely decoupled manners (Figure 8b; Movie 1, Supporting Information). These results demonstrated the importance of a high dielectric value in effectively storing electric energies.

The frequencies of most biomechanical energy, such as the finger-bending movement herein, are below 1 Hz and exceeded our measurement limit. The dielectric performance of the film at higher frequencies, such as in the testing range, can be used to predict the trends in lower frequencies because the mechanism for the dielectric behavior in our film (interfacial polarization) remained valid for lower frequency ranges. Dielectric constants generally increase with decreasing frequencies,[29,39,45,46] and films with relatively high dielectric constants in high-frequency ranges will outperform others in the low frequency ranges as well.

We also tried to increase the piezoelectric properties of the film by elongating the film by four times. Such elongation leads to a remarkable increase of β phase from 42% to 84%, and the current generated by a finger movement accordingly enhanced from 36 to 80 nA (Figure S3, Supporting Information). However, the dielectric constant dramatically decreased to less than 20 (data not shown). The possibly reason for the deterioration of the dielectric performance might be induced

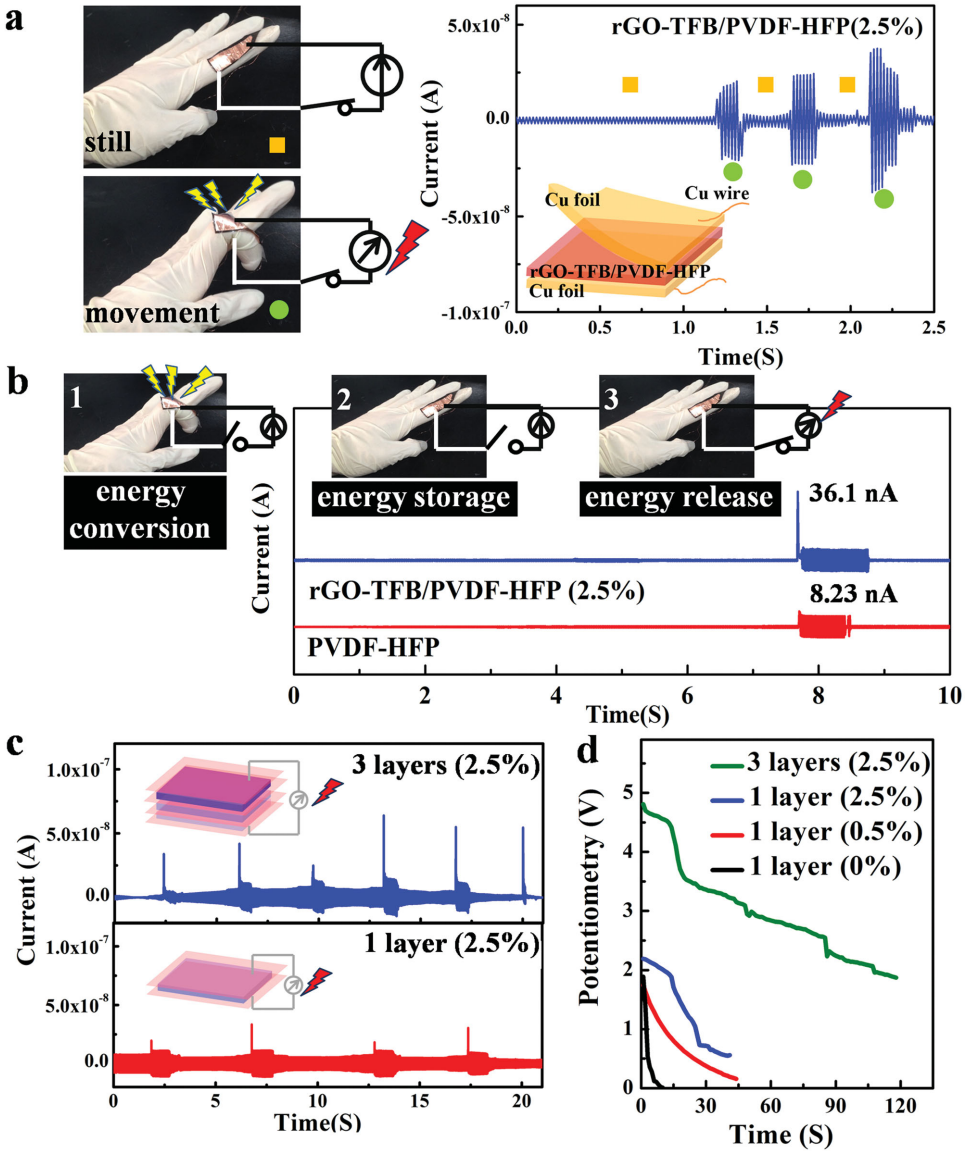

Figure 8. Output currents/voltages measurements by finger-bending motion. a) The rGO-TFB/PVDF-HFP (2.5%) under finger-bending motion, b) output current–time curve of a rGO-TFB/PVDF-HFP (2.5%) under finger-bending motion, c) output current measurements for rGO-TFB/PVDF-HFP (2.5%) after the finger-bending motion with a different numbers of layers under finger-bending motion, and d) output voltage–time curve of PVDF-HFP and rGO-TFB/PVDF-HFP (0.5 and 2.5 wt%) with a different number of layers after finger-bending motion.

by the dislocation and aggregation of the fillers during elongation, which in turn damaged the microcapacitors within the film. Such mutual restriction relationship between piezoelectric and dielectric properties calls for further studies to optimize the device performance as a electric generator–capacitor unit for specific application purposes.

2.6. Accumulating Energy in a Series of Dual Role Devices

More interesting is that when the devices were connected in a series, the output power could be accumulated. One device in the circuit typically generated a pulse current of 30 nA corresponding to the finger-bending motion, and three devices in a series generated a pulse current of 50 nA. One possible reason that the output current did not increase linearly with the number of serially connected devices is that, as the power generating ability increased with the growth of the number of devices, the circuit resistance also increased. Not only did the in situ measured current increase as the number of serially connected devices increased but also the output power density of stored electric energy remarkably increased from 33 to 120 nW cm^{-2} as calculated by the currents and voltage as shown in Figure 8c,d.

In response to the finger-bending motion movements, three serially connected devices presented an open-circuit voltage of 4.8 V and decreased gradually with the lapse of time. For the single device (2.5% rGO-TFB/PVDF-HFP), the open-circuit

voltage was 2.2 V, and the values of the voltage deteriorated faster than that of the three devices serially connected. In addition, the open-circuit voltage for the pure PVDF-HFP film or the composite film with a lower filler fraction (0.5% rGO-TFB/PVDF-HFP) decreased more rapidly with time. Longer term storage of the electric energy should be possible by using a PET (polyethylene terephthalate) film to package the device.[47]

These results demonstrated that we have achieved a functionally integrated device that can harvest low-frequency random (bio) mechanical movements as well as store the electric energy in situ. The stored electric power could be accumulated in serially connected devices, and thus, in theory, even larger electric energy could be realized by increasing the number of serially connected devices. The ability to store the electric energy allows the collection of biomechanical energy that is generated by nonsynchronous movements. This concept of accumulating small amounts of electric energy for larger electric export is similar to the phenomenon observed in electric eels (*Electrophorus electricus*). Their abdominal organs are made up of thousands of electrocytes, lined up so a current of ions can run through them. Although the voltage drop in each electrocyte is as small as 150 mV, the accumulated voltage could reach 860 V and issued by the eel for hunting, self-defense, and communicating with fellow eels.

The possibility to use our device for high energy output is currently under investigation in our lab. The decoupled electric conversion process and electric output process allowed by the energy storage ability of our flexible high-*k*–low-loss composite film will also be potentially applied to sensors.[1,2,14,48] Corresponding exploration is underway in our lab. In the meantime, performance optimizations of our film still need further studies. For example, because of the mutual restriction relationship between the piezoelectric and dielectric properties of the film fabricated by our method, we need to optimize or balance piezoelectric/dielectric performance for specific application purposes, and hopefully innovations in film fabrication methods will break this mutual restriction relationship. Other possible questions would be, what's the meaning of the values of dielectric loss in applications: does a high loss means larger voltage drop during energy output, or does it mean that the electric energy could be stored in shorter period of time, or maybe both? How a high dielectric loss will counter effect a high dielectric constant in real applications? Hopefully our current study will inspire and motivate further studies to address these issues, which will provide a better understanding of the integrated electric generator–capacitor film. If the films were to be applied as wearable devices, their mechanical performance and enduration should also be studied.

3. Conclusion

We achieved an all-solid-state flexible generator–capacitor polymeric composite film that converted low-frequency biomechanical energy into stored electric energy. This combined generator–capacitor design was realized by employing PVDF-HFP in the dual role of both the piezoelectric generator and polymer matrices in a flexible capacitor. Proper surface modification of the rGO fillers was indispensable in achieving the superior energy-storage performance of the films. Once the rGO surfaces were optimally modified, a dielectric constant of 158 and a low loss of 0.42 (100 Hz) were achieved. The film device allowed timely decoupled motion-energy harvest and output of the motion-generated electricity. Based on our report, by including the accumulation of low-frequency random biological motions, future design possibilities in the fields of motion sensors, information storage, and high-voltage output will hopefully appear in the near future.

4. Experimental Section

Materials: Natural flake graphite (300 mesh) was provided by the Shuangxing graphite processing plant, China. PVDF-HFP (density 1.78 g cm^{-3}, 5%–20% molar of hexafluoropropene), methyl pentafluorobenzoate (≥99%), and sodium azide (NaN_3, ≥99.5%) were purchased from Sigma-Aldrich. Potassium persulfate (KPS, ≥99.5%), phosphorus pentoxide (PPO, ≥98%), potassium permanganate ($KMnO_4$, ≥99.5%), sulfuric acid (H_2SO_4, 95%–98%), hydrochloric acid (HCl, 36%–38%), perhydrol (H_2O_2, 30%), and *N*,*N*-dimethyl formamide (DMF, ≥99.5%)acetone (≥99.5%), methanol (≥99.5%), and chloroform (≥99.0%) were obtained from local commercial sources and used as received.

The Preparation of TFB: Ester Methyl 4-Azidotetraflourobenzoate: A mixture of 0.30 g of NaN_3 and 0.88 g of methyl pentafluorobenzoate in acetone (8 mL) and water (3 mL) was refluxed for 8 h. The mixture was cooled, diluted with water (10 mL), and then extracted by ether (30 mL). The extract was dried ($MgSO_4$) and evaporated to leave of pale yellow liquid which solidified at standing. ^{1}H-NMR of ester methyl 4-azidotetraflourobenzoate is shown in Figure S5 in the Supporting Information.[31] A solution of 0.586 g of methyl pentafluorobenzoate with 20% aqueous NaOH (0.8 mL) in MeOH (10 mL) and water (1 mL) was stirred at 25 °C for 8 h. The solution was acidified by HC1 in an ice bath to pH <1 and extracted by $CHC1_3$ (3 × 10 mL). The extract was dried ($MgSO_4$) and evaporated to leave TFB as a colorless solid.

Preparation of rGO-TFB and N-GO-TFB: An additional graphite oxidation procedure was used, and the preoxidized graphite was prepared by KPS and PPO in concentrated H_2SO_4.[49] Then, this preoxidized graphite was subjected to oxidation by Hummers' method to prepare to GO.[50] Next, 0.05 g GO and 0.25 g TFB were mixed and heated for 40 min, and subsequently the mixture of rGO-TFB were washed by ethanol to remove extra TFB. Finally, the rGO-TFB was obtained and dried at 40 °C. The sample of noncovalently modified GO with F (N-GO-F) was prepared with the same method except that the mixture was not heated up to 140 °C but kept at room temperature for 40 min. GO was partially reduced during the covalent modification process.

Preparation of Composite Film: A measured amount of rGO-TFB(N-GO-TFB) was loaded in a 100 mL round-bottom flask and DMF (20 mL) was added. The dispersion was sonicated using a SB-5200 DTDN ultrasonic bath cleaner (160 W, Ningbo Scientz Biotechnology Co., Ltd., China) for 3 h to form a homogeneous suspension. After mixing with PVDF-HFP particles (3 g) and stirring at 80 °C for 2 h, the rGO-TFB/PVDF-HFP (N-GO-F/PVDF-HFP) solution was obtained. The as-prepared rGO-TFB/PVDF-HFP (N-GO-F/PVDF-HFP) solution was drop casted onto a glass plate and kept in an oven at 80 °C for 3 h to evaporate the solvent and then kept in an oven at 220 °C for 1 h to obtain the rGO-PEI/PVDF-HFP (N-rGO-PEI/PVDF-HFP) composite films. Due to the 220 °C film preparation processes, the GO in PVDF-HFP was reduced further.

Characterization of rGO-TFB and rGO-TFB/PVDF-HFP: The morphology of rGO-TFB was examined by SEM measurements, and elemental scanning was carried out on an EVO MA25 instrument at 20.0 kV. The chemical structures of rGO-TFB were examined by FTIR (PerkinElmer Spectrum 100) and XPS measurements were conducted using a Kratos Axis Ultra system with a monochromatized Al Kα radiation at 1486.6 eV as the X-ray source. The compatibility of rGO-TFB in PVDF-HFP was studied by (1) thermogravimetric analysis conducted on a TA Q500 at a heating rate of 10 °C min^{-1} in a nitrogen atmosphere, (2) DSC measurements which were conducted on a DSC Q2000

instrument at temperatures between 20 and 200 °C and a heating/cooling rate of 10 °C min^{-1} under a nitrogen atmosphere (the flow rate of purge gas is 50 mL min^{-1}), 3) SEM, and 4) FTIR.

The dielectric properties were determined by an impedance analyzer (Agilent 4294 A) at frequencies ranging from 10^2 to 10^6 Hz. The film strips were cut accurately from the samples. Prior to the measurement, silver electrodes were fabricated on the sides of these strips using conductive silver paint (Agar no. 0443). The mechanical response measurements were carried out on an electrochemical workstation (PGSTAT 302N, Metrohm Autolab B.V.). The rGO-TFB/PVDF-HFP were integrated with contact electrodes (Cu foil) on the upper and lower surfaces, whose electrodes were connected to an electrochemical workstation.

Supporting Information

Supporting Information is available from the Wiley Online Library or from the author.

Acknowledgements

This work was supported by the NSFC (21303169, 51572246), the Fundamental Research Funds for the Central Universities (2652014056, 2652013115), Beijing Nova Program (Z141103001814064), Beijing Specific Project to Foster Elitist (2013D009015000001), Open Project of State Key Laboratory of Chemical Resource Engineering (CRE-2013-C-201), and the Beijing Key Laboratory of Materials Utilization of Nonmetallic Minerals and Solid Waste (the project of Beijing Municipal Science and Technology Commission, No. BZ0292).

Received: August 19, 2015
Revised: September 13, 2015
Published online: October 15, 2015

[1] C. Dagdeviren, Y. W. Su, P. Joe, R. Yona, Y. H. Liu, Y. S. Kim, Y. A. Huang, A. R. Damadoran, J. Xia, L. W. Martin, Y. G. Huang, J. A. Rogers, *Nat. Commun.* **2014**, *5*, 4496.
[2] L. Persano, C. Dagdeviren, Y. W. Su, Y. H. Zhang, S. Girardo, D. Pisignano, Y. G. Huang, J. A. Rogers, *Nat. Commun.* **2013**, *4*, 1633.
[3] M. M. Song, M. J. Cheng, G. N. Ju, Y. J. Zhang, F. Shi, *Adv. Mater.* **2014**, *26*, 7059.
[4] S. Siddiquia, D. Kim, L. T. Duy, M. T. Nguyen, S. Muhammad, W. S. Yoon, N. E. Lee, *Nano Energy* **2015**, *15*, 177.
[5] C. K. Jeong, J. Lee, S. Han, J. Ryu, G. T. Hwang, D. Y. Park, J. H. Park, S. S. Lee, M. Byun, S. H. Ko, K. J. Lee, *Adv. Mater.* **2015**, *27*, 2866.
[6] Y. K. Fuh, P. C. Chen, Z. M. Huang, H. C. Ho, *Nano Energy* **2015**, *11*, 671.
[7] P. Bai, G. Zhu, Z. H. Lin, Q. Jing, J. Chen, G. Zhang, J. Ma, Z. L. Wang, *ACS Nano* **2013**, *7*, 3713.
[8] J. H. Lee, K. Y. Lee, M. K. Gupta, T. Y. Kim, D. Y. Lee, J. Oh, C. Ryu, W. J. Yoo, C. Y. Kang, S. J. Yoon, J. B. Yoo, S. W. Kim, *Adv. Mater.* **2014**, *26*, 765.
[9] Z. L. Wang, W. Z. Wu, *Angew. Chem. Int. Ed.* **2012**, *51*, 11700.
[10] P. K. Yang, Z. H. Lin, K. C. Pradel, L. Lin, X. H. Li, X. N. Wen, J. H. He, Z. L. Wang, *ACS Nano* **2015**, *9*, 901.
[11] Y. L. Zi, L. Lin, J. Wang, S. H. Wang, J. Chen, X. Fan, P. K. Yang, F. Yi, Z. L. Wang, *Adv. Mater.* **2015**, *27*, 2340.
[12] J. S. Chun, N. R. Kang, J. Y. Kim, M. S. Noh, C. Y. Kang, D. Choi, S. W. Kim, Z. L. Wang, J. M. Baik, *Nano Energy* **2015**, *11*, 1.
[13] V. Eswaraiah, K. Balasubramaniam, S. Ramaprabhu, *J. Mater. Chem.* **2011**, *21*, 12626.
[14] P. Khanchaitit, K. Han, M. R. Gadinski, Q. Li, Q. Wang, *Nat. Commun.* **2013**, *4*, 2845.
[15] J. B. Goodenough, K. S. Park, *J. Am. Chem. Soc.* **2013**, *135*, 1167.
[16] M. V. Reddy, G. V. Subba Rao, B. V. R. Chowdari, *Chem. Rev.* **2013**, *113*, 5364.
[17] G. M. Zhou, F. Li, H. M. Cheng, *Energy Environ. Sci.* **2014**, *7*, 1307.
[18] S. H. Liu, Z. Y. Wang, C. Yu, H. B. Wu, G. Wang, Q. Dong, J. S. Qiu, A. Eychmüller, X. W. Lou, *Adv. Mater.* **2013**, *25*, 3462.
[19] K. Wang, H. P. Wu, Y. N. Meng, Z. X. Wei, *Small* **2014**, *10*, 14.
[20] X. F. Wang, B. Liu, Q. F. Wang, W. F. Song, X. J. Hou, D. Chen, Y. B. Cheng, G. Z. Shen, *Adv. Mater.* **2013**, *25*, 1479.
[21] S. H. Wang, Z. H. Lin, S. M. Niu, L. Lin, Y. N. Xie, K. C. Pradel, Z. L. Wang, *ACS Nano* **2013**, *7*, 11263.
[22] X. Y. Xue, P. Deng, B. He, Y. X. Nie, L. L. Xing, Y. Zhang, Z. L. Wang, *Adv. Energy Mater.* **2014**, *4*, 1301329.
[23] A. Ramadoss, B. Saravanakumar, S. W. Lee, Y. S. Kim, S. J. Kim, Z. L. Wang, *ACS Nano* **2015**, *9*, 4337.
[24] K. Yang, X. Y. Huang, L. J. Fang, J. L. He, P. K. Jiang, *Nanoscale* **2014**, *6*, 14740.
[25] W. S. Tong, Y. H. Zhang, Q. Zhang, X. L. Luan, Y. Duan, S. F. Pan, F. Z. Lv, Q. An, *Carbon* **2015**, *94*, 590.
[26] Y. Q. Chen, B. P. Lin, X. Q. Zhang, J. C. Wang, C. W. Lai, Y. Sun, Y. R. Liu, H. Yang, Chen, *J. Mater. Chem. A* **2014**, *2*, 14118.
[27] J. W. Shang, Y. H. Zhang, L. Yu, X. L. Luan, B. Shen, Z. L. Zhang, F. Z. Lv, P. K. Chu, *J. Mater. Chem. A* **2013**, *1*, 884.
[28] D. R. Wang, Y. Bao, J. W. Zha, J. Zhao, Z. M. Dang, G. H. Hu, *ACS Appl. Mater. Interfaces* **2012**, *4*, 6273.
[29] C. Wu, X. Y. Huang, G. L. Wang, X. F. Wu, K. Yang, S. T. Li, P. K. Jiang, *J. Mater. Chem.* **2012**, *22*, 7010.
[30] A. M. Abuelela, R. S. Farag, T. A. Mohamed, O. V. Prezhdo, *J. Phys. Chem. C* **2013**, *117*, 19489.
[31] J. F. W. Kean, S. X. Cai, *J. Org. Chem.* **1990**, *55*, 3640.
[32] L. H. Liu, G. Zorn, D. G. Castner, R. Solanki, M. M. Lernerd, M. D. Yan, *J. Mater. Chem.* **2010**, *20*, 5041.
[33] C. Min, D. M. Yu, J. Y. Cao, G. L. Wang, L. H. Feng, *Carbon* **2013**, *55*, 116.
[34] M. Pumera, H. Iwai, *J. Phys. Chem. C* **2009**, *113*, 4401.
[35] L. H. Liu, M. D. Yan, *Acc. Chem. Res.* **2010**, *43*, 1434.
[36] L. H. Liu, M. D. Yan, *Nano Lett.* **2009**, *9*, 3375.
[37] M. Holzinger, J. Abraham, P. Whelan, R. Graupner, L. Ley, F. Hennrich, M. Kappes, A. Hirsch, *J. Am. Chem. Soc.* **2003**, *125*, 8566.
[38] L. H. Liu, M. M. Lerner, M. D. Yan, *Nano Lett.* **2010**, *10*, 3754.
[39] J. Y. Kim, W. H. Lee, J. W. Suk, J. R. Potts, H. Chou, I. N. Kholmanov, R. D. Piner, J. Lee, D. Akinwande, R. S. Ruoff, *Adv. Mater.* **2013**, *25*, 2308.
[40] W. S. Tong, Y. H. Zhang, L. Yu, X. L. Luan, Q. An, Q. Zhang, F. Z. Lv, P. K. Chu, B. Shen, Z. L. Zhang, *J. Phys. Chem. C* **2014**, *118*, 10567.
[41] A. B. Bourlinos, V. Georgakilas, R. Zboril, T. A. Steriotis, A. K. Stubos, *Small* **2009**, *5*, 1841.
[42] V. Tomer, E. Manias, C. A. Randall, *J. Appl. Phys.* **2011**, *110*, 044107.
[43] X. J. He, K. Yao, B. K. Gan, *J. Appl. Phys.* **2005**, *97*, 084101.
[44] K. Yang, X. Y. Huang, Y. H. Huang, L. Y. Xie, P. K. Jiang, *Chem. Mater.* **2013**, *25*, 2327.
[45] C. W. Nan, Y. Shen, J. Ma, *Annu. Rev. Mater. Res.* **2010**, *40*, 131.
[46] Z. M. Dang, L. Wang, Y. Yin, Q. Zhang, Q. Q. Lei, *Adv. Mater.* **2007**, *19*, 852.
[47] C. T. Pan, C. K. Yen, H. C. Wu, L. W. Lin, Y. S. Lu, J. C. C. Huang, S. W. Kuo, *J. Mater. Chem. A* **2015**, *3*, 6835.
[48] G. Schwartz, B. C. Tee, J. G. Mei, A. L. Appleton, D. H. Kim, H. L. Wang, Z. N. Bao, *Nat. Commun.* **2013**, *4*, 1895.
[49] W. Hummers, R. Offeman, *J. Am. Chem. Soc.* **1958**, *80*, 1339.
[50] N. I. Kovtyukhova, P. J. Ollivier, B. R. Martin, T. E. Mallouk, S. A. Chizhik, E. V. Buzaneva, A. D. Gorchinskiy, *Chem. Mater.* **1999**, *11*, 771.